ACS APPLIED MATERIALS & INTERFACES

www.acsami.org

Research Article

"Lewis Base-Hungry" Amorphous–Crystalline Nickel Borate–Nickel Sulfide Heterostructures by In Situ Structural Engineering as Effective Bifunctional Electrocatalysts toward Overall Water Splitting

Zemin Sun, Xiaorui Wang, Mengwei Yuan, Han Yang, Yuhe Su, Kefan Shi, Caiyun Nan, Huifeng Li, Genban Sun,* Jia Zhu,* Xiaojing Yang, and Shaowei Chen*

Cite This: *ACS Appl. Mater. Interfaces* 2020, 12, 23896–23903

Read Online

ACCESS | Metrics & More | Article Recommendations | Supporting Information

ABSTRACT: The development of high-performance, low-cost, and long-lasting electrocatalysts for both hydrogen evolution reaction (HER) and oxygen evolution reaction (OER) is urgently needed for effective electrochemical water splitting. In the present study, an engineering process was employed to prepare "Lewis base-hungry" amorphous–crystalline nickel borate–nickel sulfide ($Ni_3(BO_3)_2$–Ni_3S_2) heterostructures, which exhibited unprecedentedly high electrocatalytic activity toward both OER and HER in alkaline media. The optimal $Ni_3(BO_3)_2$–Ni_3S_2/nickel foam ($Ni_3(BO_3)_2$–Ni_3S_2/NF) electrode displayed an ultralow overpotential of only −92 and +217 mV to reach the current density of 10 mA cm^{-2} for HER and OER, respectively. When the $Ni_3(BO_3)_2$–Ni_3S_2/NF electrode was used as both the anode and cathode for overall water splitting, a low cell voltage of 1.49 V was needed to achieve the current density of 10 mA cm^{-2}, which was superior to the performance of most noble metal-free electrocatalysts. Results from density functional theory calculations showed that the Lewis base-hungry sites in the heterostructures effectively enhanced the chemisorption of hydrogen and oxygen intermediates, a critical step in HER and OER electrocatalysis. Results from this study highlight the significance of rational design and engineering of heterostructured materials for the development of high-efficiency electrocatalysts.

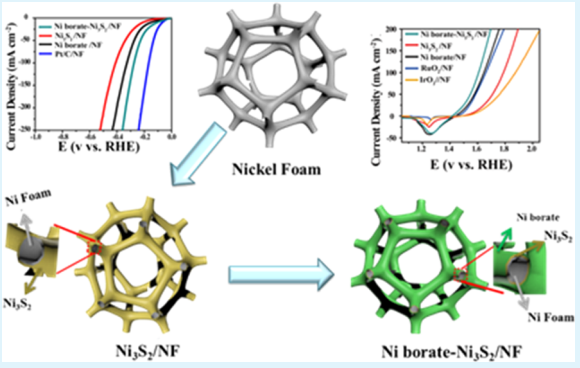

KEYWORDS: *amorphous–crystalline heterostructure, Lewis acid–base interaction, S vacancy, bifunctional electrocatalyst, overall water splitting*

INTRODUCTION

Development of clean and sustainable energy technologies has been attracting extensive interest in light of the rapid depletion of fossil fuels and the environmental impacts by the combustion of fossil fuels.[1,2] Hydrogen has been recognized as a green energy source,[3,4] and water splitting is a viable technology for hydrogen production.[5,6] There are two major reactions in electrochemical water splitting, hydrogen evolution reaction (HER) at the cathode and oxygen evolution reaction (OER) at the anode, and effective catalysts are needed to boost the electron-transfer kinetics for both reactions so as to achieve a sufficiently high current density for practical applications.[6,7] Noble metal-based materials (e.g., Pt, Au, Ru, and Ir) have been the catalysts of choice for these reactions. For instance, Pt-based nanoparticles are the leading electrocatalysts for HER, while Ir- and Ru-based nanoparticles for OER.[8,9] Yet, the high costs and low natural abundance of these noble metals have hampered the widespread application of the technology. Therefore, it is of fundamental and technological significance to develop low-cost alternative catalysts from earth-abundant elements that exhibit high activity and durability for HER and OER.[6]

Thus far, a range of nonnoble metal catalysts have been tested for electrocatalytic water splitting, such as compounds of transition metals such as cobalt, nickel, and iron.[10−14] In fact, Ni-based materials are promising catalysts for HER and OER.[14,15] Among these, Ni_3S_2 is of particular interest because it exhibits high intrinsic electrical conductivity,[16] and its electrocatalytic activity can be enhanced by various structural variables. For instance, doping with select metal elements (e.g.,

Received: February 27, 2020
Accepted: May 4, 2020
Published: May 4, 2020

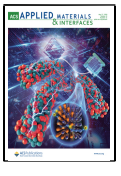

https://dx.doi.org/10.1021/acsami.0c03796
ACS Appl. Mater. Interfaces 2020, 12, 23896–23903

Fe, V, and Mo) can lead to an increase in the number of active sites, enhanced electrical conductivity, and optimized adsorption/desorption energetics of reaction intermediates.[3,16,17] In addition, the formation of nanocomposites by structural engineering with other functional materials (such as nitrogen-doped graphene) has been found to synergistically enhance the electron-transfer kinetics on the active sites.[18] Yet, in these earlier studies, the performance enhancement is mostly limited to either HER or OER,[19,20] and it remains challenging to achieve apparent electrocatalytic activity of Ni_3S_2-based nanocomposites toward both HER and OER such that they can serve as effective bifunctional electrocatalysts for overall water splitting.

One unique strategy is to produce heterostructures, where the synergistic interactions among the varied structural components can be exploited to enhance the charge transfer and eventual electrocatalytic performance. In a recent study,[21] arrays of MoS_2−Ni_3S_2 heterostructures have been found to deliver a low cell voltage ($E_{WS,10}$) of 1.56 V to reach the current density of 10 mA cm^{-2} in water splitting. A similar performance was observed with heterostructured arrays of a core−shell Ni_3S_2@MoS_2/FeOOH ($E_{WS,10}$ = 1.57 V)[22] and $NiCo_2O_4$−$CoMoO_4$ ($E_{WS,10}$ = 1.55 V).[23] Notably, in these earlier studies, the catalysts consist mostly of crystalline−crystalline heterostructures. Yet, in practice, the self-reconstruction of crystalline materials is sluggish, rendering it a tedious process to produce heterostructured catalysts. In contrast, heterostructured arrays with amorphous materials can be facilely produced, primarily because amorphous materials possess the advantageous features of rapid cation diffusion and low energy costs for vacancy formation, which are conducive to high-performance electrocatalysis.[24,25] However, thus far reports have been scarce in the preparation of amorphous−crystalline heterostructures.

Notably, during water splitting, one important step is the adsorption of oxygen-containing intermediates (e.g., water, hydroxide) onto the catalyst surface. As these intermediates behave analogously to Lewis bases with lone-pair electrons,[13,14] their adsorption onto the catalyst surface can be enhanced by boration engineering of the catalysts producing Lewis acid sites, eventually leading to enhanced water splitting performance.[13,14,26] Herein, a facile low-temperature hydrothermal procedure is described for the in situ engineering construction of nickel foam-supported electrodes based on "Lewis base-hungry" amorphous−crystalline $Ni_3(BO_3)_2$−Ni_3S_2/NF heterostructures. The obtained nanocomposites exhibited an outstanding and robust activity toward both HER and OER in alkaline media. The optimal electrode displayed an ultralow overpotential (η_{10}) of only −92 and +217 mV at 10 mA cm^{-2} for HER and OER, respectively. The performance was markedly better than those of single-component amorphous $Ni_3(BO_3)_2$/NF (−98 and +245 mV) and single-component crystalline Ni_3S_2/NF (−194 and +358 mV). The improved performance of $Ni_3(BO_3)_2$−Ni_3S_2/NF is ascribed to the following factors: (1) abundant S vacancies at the interface between Ni_3S_2 and $Ni_3(BO_3)_2$ that facilitated the transformation of H_{ads} into H_2;[16,17] (2) enhanced adsorption of oxygen-containing Lewis base intermediates by $Ni_3(BO_3)_2$ onto $Ni_3(BO_3)_2$−Ni_3S_2/NF due to Lewis acid−base interactions; and (3) increased electrical conductivity of the electrode due to the highly conductive, three-dimensional nickel foam. Remarkably, the heterostructured nanocomposites served as effective catalysts toward overall water splitting, with a low $E_{WS,10}$ of only 1.49 V, which remained virtually invariant for more than 60 h of continuous operation. This represents one of the best noble metal-free electrocatalysts for water splitting.

EXPERIMENTAL SECTION

Preparation of Ni_3S_2/NF, $Ni_3(BO_3)_2$−Ni_3S_2/NF, and $Ni_3(BO_3)_2$/NF Electrodes. The electrodes were synthesized by a facile hydrothermal method. In brief, 80 mL of an aqueous solution containing 0.1 g thiourea was transferred into a poly(tetrafluorethylene)-lined stainless steel autoclave; then a piece of Ni foam (2 cm × 2 cm) was placed into the solution. The autoclave was heated at 120 °C in an electric oven for 6 h and then allowed to cool naturally to room temperature, producing Ni_3S_2/NF. The obtained Ni_3S_2/NF was then subjected to a second hydrothermal reaction in a saturated borax solution for 12 and 48 h, producing $Ni_3(BO_3)_2$−Ni_3S_2/NF and $Ni_3(BO_3)_2$/NF, respectively.

Preparation of RuO_2/NF, IrO_2/NF, and Pt/C/NF Electrodes. RuO_2 (5 mg) was dispersed in a 1 mL mixed solution (490 μL water, 15 μL 5 wt % Nafion solution, and 495 μL ethanol), followed by sonication to obtain a catalyst ink. The catalyst ink (100 μL) was then dropcast on the surface of nickel foam (2 cm × 2 cm), which was dried at 80 °C overnight. IrO_2/NF and Pt/C/NF electrodes were prepared in a similar fashion. The catalyst loading (RuO_2, IrO_2, Pt/C) was all ca. 0.5 mg cm^{-2}.

Characterization. Inductively coupled plasma-atomic emission spectroscopy (ICP-AES) measurements were carried out with a Shimadzu ICPE-9820 instrument. X-ray diffraction (XRD) patterns were acquired with a Phillips X'pert ProMPD diffractometer (Cu Kα, λ = 1.54056 Å) at 40 kV and 40 mA. X-ray photoelectron spectra (XPS) were collected with a Thermo Fisher ESCALAB 250Xi spectrometer with Al Kα radiation. Field-emission scanning electron microscopic (FESEM) images were obtained with a Hitachi scanning electron microscope operated at the acceleration voltage of 10 kV. Transmission electron microscopy (TEM) images were collected with an FEI Tecnai F20 transmission electron microscope at the acceleration voltage of 200 kV. Electron spin resonance (ESR) spectra were obtained with a JEOL JESX320 spectrometer at the frequency of 9.184 GHz at room temperature.

Electrochemistry. Electrochemical measurements were performed with a Zennium IM6 electrochemical analyzer in a standard three-electrode system (a Pt wire as the counter electrode for OER and a graphite rod as the counter electrode for HER, Hg/HgO electrode as the reference electrode, and as-prepared NF-supported composites as the working electrode). The Hg/HgO reference electrode was calibrated against a reversible hydrogen electrode (RHE) (Figure S1), according to the following formula: $E_{RHE} = E_{Hg/HgO} + 0.098 + 0.0591$ pH, and all potentials in the present study were referenced to this RHE. The performance was tested in 1.0 M KOH by linear sweep voltammetry (LSV) at the scan rate of 2 mV s^{-1} for HER and 5 mV s^{-1} for OER. Electrochemical impedance spectroscopy (EIS) studies were carried out at the AC amplitude of 5 mV within the frequency range of 0.01 Hz to 100 kHz in a 1.0 M KOH solution.

Theoretical Calculations. Density functional theory (DFT) calculations were performed using Vienna ab initio simulation package (VASP) code within the projector augmented wave (PAW) method. The generalized gradient approximation (GGA) with the Perdew−Burke−Ernzerhof (PBE) exchange−correlation functional was adopted to examine the electronic exchange−correlation function of the interacting electrons. A 400 eV kinetic energy cutoff was used for the plane-wave expansion. The convergence of forces was set to 0.02 eV $Å^{-1}$. A Fermi smearing of 0.1 eV was used to ensure the fast convergence of the self-consistent electron density. A vacuum layer of 15 Å was applied for all calculated models to avoid the interaction between the periodic images. In the structural models for $Ni_3(BO_3)_2$ and Ni_3S_2 surfaces, the slab thickness was about 9 Å. The $Ni_3(BO_3)_2$−Ni_3S_2 composite was constructed by attaching $Ni_3(BO_3)_2$(001) and Ni_3S_2(001) surfaces together, at a lattice mismatch of about 4.1%. The

https://dx.doi.org/10.1021/acsami.0c03796
ACS Appl. Mater. Interfaces 2020, 12, 23896−23903

Brillouin zone was sampled using a 1 × 4 × 1 Monkhorst−Pack grid. Additional details are included in the Supporting Information.

RESULTS AND DISCUSSION

The preparation of the Ni_3S_2/NF, $Ni_3(BO_3)_2$−Ni_3S_2/NF, and $Ni_3(BO_3)_2$/NF electrodes is schematically illustrated in Scheme 1, which involves two major steps. (a) A Ni_3S_2 nanoparticle layer (yellow) was grown onto Ni foam (Ni_3S_2/NF) by a low-temperature hydrothermal route, where the nickel foam worked as both the substrate and the Ni ion source; and (b) the Ni_3S_2 nanoparticles were then partly converted into amorphous $Ni_3(BO_3)_2$ (green) in a second hydrothermal treatment with the addition of sodium borate, producing $Ni_3(BO_3)_2$−Ni_3S_2 heterostructures. Notably, when the hydrothermal time was prolonged from 12 to 48 h, Ni_3S_2 was completely converted to amorphous $Ni_3(BO_3)_2$, leading to the formation of $Ni_3(BO_3)_2$/NF instead. From ICP-AES measurements (Table S1), the loading of catalysts was estimated to be ca. 0.20 mg cm^{-2}, where the boron content increased and concurrently sulfur content decreased with the reaction time increasing from 0 to 48 h, suggesting in situ chemical reactions from Ni_3S_2 to $Ni_3(BO_3)_2$ under the sodium borate hydrothermal condition.

Scheme 1. Schematic Illustration of the Fabrication of the Ni_3S_2/NF, $Ni_3(BO_3)_2$−Ni_3S_2/NF, and $Ni_3(BO_3)_2$/NF Electrodes

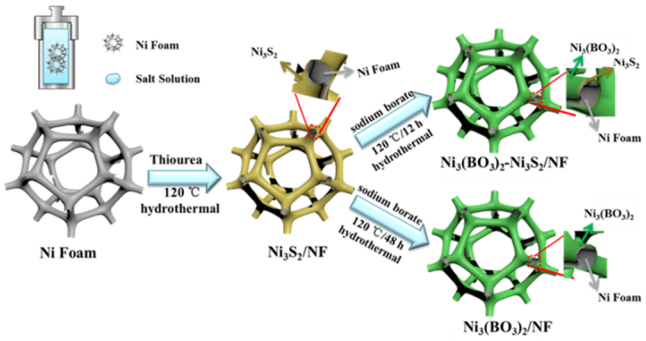

The structures of the samples were first characterized by XRD measurements. Figure 1a shows the XRD patterns of Ni foam, Ni_3S_2/NF, $Ni_3(BO_3)_2$/NF, and $Ni_3(BO_3)_2$−Ni_3S_2/NF. Five peaks can be identified with the Ni_3S_2/NF sample (black curve) at 2θ = 21.7, 31.1, 37.8, 49.7, and 55.2°, which can be indexed to the (101), (110), (003), (113), and (122) diffractions of Ni_3S_2 (JCPDS No. 44-1418), respectively, whereas the three major peaks (marked by asterisks) at 2θ = 44.5, 51.8, and 76.4° are due to the NF substrate (Figure S2).[7] Notably, the $Ni_3(BO_3)_2$−Ni_3S_2/NF sample (red curve) retained the diffraction patterns of Ni_3S_2 without any other peaks, whereas the diffraction patterns of $Ni_3(BO_3)_2$/NF (blue curve) are consistent with those of Ni foam alone, and the disappearance of the Ni_3S_2 diffraction peaks after 48 h of hydrothermal reaction indicates that Ni_3S_2 was completely converted to amorphous $Ni_3(BO_3)_2$.

The chemical composition of the samples was then examined by XPS measurements. From the XPS survey spectra in Figure 1b, one can see that the S 2p peak (ca. 163 eV) diminished, whereas the B 1s peak (ca. 192 eV) increased, in intensity from Ni_3S_2/NF (black curve) to $Ni_3(BO_3)_2$−Ni_3S_2/NF (red curve) and to $Ni_3(BO_3)_2$/NF (blue curve), suggesting the successful transformation of Ni_3S_2 to $Ni_3(BO_3)_2$. The high-resolution scans of the Ni 2p electrons for Ni_3S_2/NF, $Ni_3(BO_3)_2$−Ni_3S_2/NF, and $Ni_3(BO_3)_2$/NF are depicted in Figure 1c. Deconvolution yields two doublets for the $Ni_3(BO_3)_2$−Ni_3S_2/NF sample, one at 855.3 and 874.1 eV due to the $2p_{3/2}$ and $2p_{1/2}$ electrons of Ni^{2+}, and the other at 856.8 and 874.7 eV to Ni^{3+}.[27−29] With prolonged hydrothermal time, the Ni 2p binding energy can be seen to show a negative shift, suggesting effective regulation of the electron density on the Ni centers with the anion transformed from S^{2-} to borate.[30,31] In the S 2p spectrum of $Ni_3(BO_3)_2$−Ni_3S_2/NF (Figure 1d), the peaks at 162.1 and 163.2 eV can be assigned to the S $2p_{3/2}$ and $2p_{1/2}$ electrons of bridging S_2^{2-}, and these binding energies are somewhat lower than those of Ni_3S_2, suggesting the formation of an increasing number of S vacancies.[15,31−33] This is likely due to the formation of amorphous $Ni_3(BO_3)_2$ layers, where the reduced crystallinity enhanced unsaturated coordination at the interface. The $Ni_3(BO_3)_2$−Ni_3S_2/NF sample also shows a peak at 168.3 eV that can be ascribed to SO_4^{2-} species, again, indicating strong

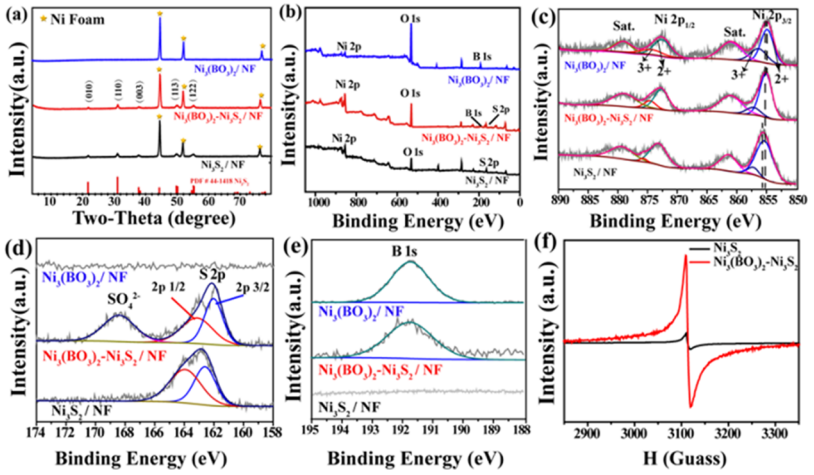

Figure 1. (a) XRD patterns of Ni_3S_2/NF, $Ni_3(BO_3)_2$−Ni_3S_2/NF, and $Ni_3(BO_3)_2$/NF. (b) XPS survey spectra of Ni_3S_2/NF, $Ni_3(BO_3)_2$−Ni_3S_2/NF, and $Ni_3(BO_3)_2$/NF. High-resolution XPS spectra of the (c) Ni 2p, (d) S 2p, and (e) B 1s electrons in Ni_3S_2/NF, $Ni_3(BO_3)_2$−Ni_3S_2/NF, and $Ni_3(BO_3)_2$/NF. (f) Room-temperature ESR spectra of the Ni_3S_2 and $Ni_3(BO_3)_2$−Ni_3S_2 samples.

https://dx.doi.org/10.1021/acsami.0c03796
ACS Appl. Mater. Interfaces 2020, 12, 23896−23903

cation interactions at the interface. The formation of borate species in the sample is manifested by the peak at 191.7 eV due to the B 1s electrons (Figure 1e).[34]

The formation of an increasing number of S vacancies in $Ni_3(BO_3)_2$–Ni_3S_2/NF, as compared to that in Ni_3S_2/NF, is further manifested in ESR measurements. From Figure 1f, the ESR signal at g = 2.004 can be found to be markedly stronger for $Ni_3(BO_3)_2$–Ni_3S_2 than for Ni_3S_2.[29,35−37] More S vacancies would provide more empty d orbitals, which is conducive to the adsorption of oxygen-containing species, leading to enhanced catalytic activity for water splitting.[35,36]

Further structural insights were obtained in electron microscopic measurements (Figure 2). Figure 2a shows an

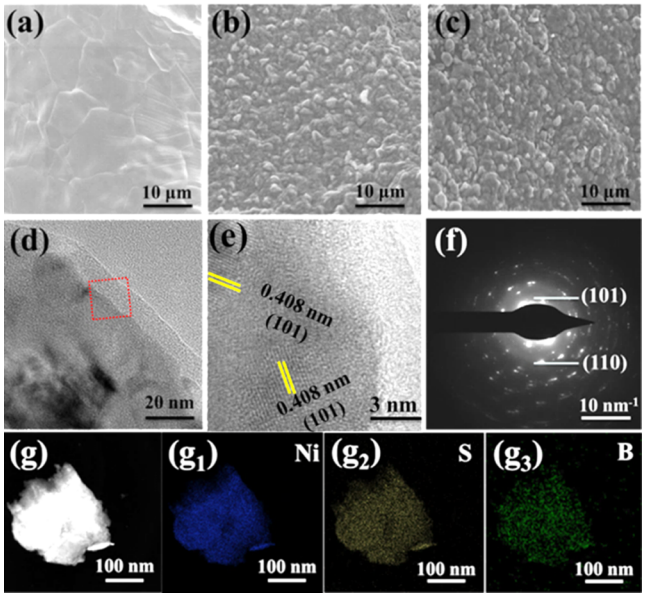

Figure 2. SEM images of (a) Ni foam, (b) Ni_3S_2/NF, and (c) $Ni_3(BO_3)_2$–Ni_3S_2/NF. (d) TEM and (e) high resolution TEM (HRTEM) images of $Ni_3(BO_3)_2$–Ni_3S_2/NF, and the corresponding (f) SAED patterns and (g) TEM–EDS elemental maps.

SEM image of commercial nickel foam, which exhibits a smooth surface. After sulfidation, the surface became roughened, due to the formation of a hierarchical nanostructure consisting of a Ni_3S_2 nanoparticle layer (Ni_3S_2/NF) (Figure 2b). The borax treatment of Ni_3S_2/NF, for up to 48 h, did not change the morphology significantly ($Ni_3(BO_3)_2$–Ni_3S_2/NF in Figure 2c and $Ni_3(BO_3)_2$/NF in Figure S3). The samples were then characterized by TEM measurements. From the TEM images in Figures 2e and S4a, one can see that the sulfidation product of Ni_3S_2 was highly crystalline, exhibiting well-defined lattice fringes with an interplanar spacing of 0.408 nm that is in good agreement with the (101) planes of Ni_3S_2 (JCPDS No. 44-1418). Consistent results were obtained in selected area electron diffraction (SAED) measurements, where the patterns (Figure 2f) can be indexed to the (101) planes of Ni_3S_2. After 12 h of borax treatment, amorphous $Ni_3(BO_3)_2$ of ca. 4.0 nm in thickness was produced on the surface of Ni_3S_2 (Figure 2d), indicating the formation of amorphous–crystalline $Ni_3(BO_3)_2$–Ni_3S_2 heterostructures. With the borax treatment time increased to 48 h, the heterostructures were completely converted to pure amorphous $Ni_3(BO_3)_2$ (Figure S4b). In addition, elemental mapping analysis based on X-ray energy-dispersive spectroscopy (EDS, Figure 2g) measurements demonstrated that the elements Ni, S, and B (Figure 2g_{1-3}) were distributed uniformly within the heterostructures.

The HER activity of the as-prepared catalysts was then tested in a three-electrode system in a 1 M KOH electrolyte purged with Ar gas. The polarization curves of bare NF and Ni_3S_2/NF, $Ni_3(BO_3)_2$/NF, $Ni_3(BO_3)_2$–Ni_3S_2/NF, and commercial Pt/C/NF are shown in Figures 3a and S5, and the

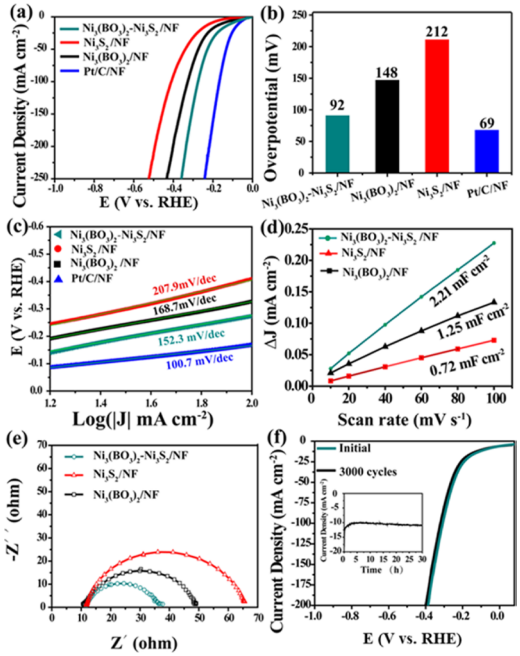

Figure 3. (a) HER polarization curves, (b) HER overpotential ($\eta_{10,HER}$) at 10 mA cm^{-2}, and (c) Tafel plots of Ni_3S_2/NF, $Ni_3(BO_3)_2$–Ni_3S_2/NF, $Ni_3(BO_3)_2$/NF, and Pt/C/NF. (d) Estimation of C_{dl}. (e) Nyquist plots of Ni_3S_2/NF, $Ni_3(BO_3)_2$–Ni_3S_2/NF, and $Ni_3(BO_3)_2$/NF. (f) Polarization curves of $Ni_3(BO_3)_2$–Ni_3S_2/NF in the first scan and after 3000 cycles in 1.0 M KOH. Inset to panel (f) shows the current–time profile at η = −85 mV in 1.0 M KOH for 30 h.

results for the samples prepared by borax treatment for up to 48 h are depicted in Figure S6a. Interestingly, for the samples prepared by borax treatment for 6–42 h, the catalytic performance was very close to that of $Ni_3(BO_3)_2$–Ni_3S_2 heterostructures (12 h), which showed the lowest overpotential among the series (Figures S6b and 3b). For instance, the overpotential ($\eta_{10,HER}$) to reach the current density of 10 mA cm^{-2} was only ca. −92 mV for $Ni_3(BO_3)_2$–Ni_3S_2/NF, substantially lower than those of $Ni_3(BO_3)_2$/NF (−148 mV) and Ni_3S_2/NF (−212 mV) and close to that (−69 mV) of Pt/C (Figure 3b). In fact, in comparison with relevant catalysts recently reported in the literature (Table S2), one can see that the as-prepared $Ni_3(BO_3)_2$–Ni_3S_2/NF was among the best.

The Tafel plots of the series of samples are shown in Figure 3c. $Ni_3(BO_3)_2$–Ni_3S_2/NF can be seen to display a Tafel slope of 152.3 mV dec^{-1}, drastically lower than those of $Ni_3(BO_3)_2$/NF (168.7 mV dec^{-1}) and Ni_3S_2/NF (207.9 mV dec^{-1}).[38,39] This suggests that HER on the three electrocatalysts was dominated by the Volmer step, in which the H_2O adsorption was a key step, and the small Tafel slope of 152.3 mV dec^{-1} for $Ni_3(BO_3)_2$–Ni_3S_2/NF indicated effective H_2O adsorption, consistent with the high catalytic activity as shown in LSV

https://dx.doi.org/10.1021/acsami.0c03796
ACS Appl. Mater. Interfaces 2020, 12, 23896−23903

measurements (Figure 3a). This can be ascribed to the increasing number of S vacancies, as manifested in XPS and ESR measurements, which produced empty d orbitals to facilitate the adsorption of H_2O and eventual hydrogen production.[40]

The electrocatalytic activity of samples can also be correlated with the electrochemical surface area (ECSA), which can be quantified by the double-layer capacitances (C_{dl}, Figure 3d). From cyclic voltammetry measurements (Figure S7), C_{dl} of $Ni_3(BO_3)_2$−Ni_3S_2/NF was estimated to be 2.21 mF cm^{-2}, much higher than those of Ni_3S_2/NF (0.72 mF cm^{-2}) and $Ni_3(BO_3)_2$/NF (1.25 mF cm^{-2}), suggesting exposure of and ready access to more active sites in $Ni_3(BO_3)_2$−Ni_3S_2/NF. The introduction of electron-deficient borate acted as Lewis base-hungry sites, which enhanced surface adsorption and increased the ECSA of the catalysts. Furthermore, the formation of heterostructures can enrich active sites for HER derived from the S vacancies and form Lewis base-hungry sites.

Further analysis of the HER performance was carried out where the turnover frequency (TOF) of HER at the overpotential of −300 mV was estimated and compared (details in the Supporting Information). $Ni_3(BO_3)_2$−Ni_3S_2/NF exhibited a TOF of 0.86 s^{-1}, much higher than those of $Ni_3(BO_3)_2$/NF (0.44 s^{-1}) and Ni_3S_2/NF (0.19 s^{-1}). In EIS measurements (Figures 3e and S8), it can be seen that in comparison with Ni_3S_2/NF, $Ni_3(BO_3)_2$/NF, and NF, $Ni_3(BO_3)_2$−Ni_3S_2/NF exhibited the smallest diameter of the arc, corresponding to the lowest charge-transfer resistance (R_{ct}) for the amorphous−crystalline heterostructured catalysts.[17,18]

To evaluate the stability of the catalysts, continuous CV and chronopotentiometric measurements were carried out. After 3000 CV cycles, $Ni_3(BO_3)_2$−Ni_3S_2/NF exhibited only a −12 mV shift at 200 mA cm^{-2} (Figure 3f). In the current density−time curve collected at the fixed potential of −85 mV, one can see that the current density remained virtually invariant for 30 h (inset to Figure 3f). Remarkably, the structure and morphology of the catalysts remained practically invariant after the prolonged HER measurements, as manifested in XRD, XPS (Figure S9), and SEM measurements (Figure S10).

Interestingly, the obtained samples also exhibited apparent electrocatalytic activity toward OER. Figures 4a and S9 depict the OER polarization curves from +2.0 to +1.0 V in 1.0 M KOH for bare NF, Ni_3S_2/NF, $Ni_3(BO_3)_2$/NF, and $Ni_3(BO_3)_2$−Ni_3S_2/NF at the potential sweep rate of 5 mV s^{-1} (the voltammetric peak at ca. +1.25 V is likely due to the electroreduction of the catalysts). One can see that amorphous−crystalline $Ni_3(BO_3)_2$−Ni_3S_2/NF exhibited an outstanding OER activity, with the overpotential ($\eta_{10,OER}$) to reach the current density of 10 mA cm^{-2} at +217 mV, markedly better than those of bare NF (+725 mV), $Ni_3(BO_3)_2$/NF (+263 mV), Ni_3S_2/NF (+353 mV), and even commercial IrO_2/NF (+379 mV) and RuO_2/NF (+274 mV) (Figures 4b and S11). In fact, the OER performance of the $Ni_3(BO_3)_2$−Ni_3S_2/NF sample for OER was even superior to those of leading noble metal-free electrocatalysts reported in the literature (Table S3).

The OER process involves four proton-coupled electron transfer steps.[41,42] The first step is OH electrochemical adsorption onto the active site, $* + H_2O \rightleftharpoons * + OH_{ads} + H^+ + e^-$; the second and third steps are electrochemical desorption of oxygen intermediates, $* - OH_{ads} \rightleftharpoons *- O_{ads} + H^+ + e^-$ and then $O^* + H_2O \rightarrow OOH^* + H^+ + e^-$; and the fourth step is

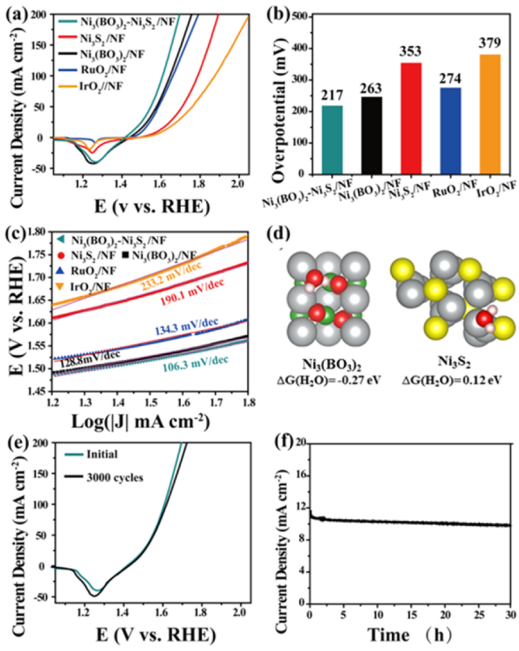

Figure 4. (a) OER polarization curves, (b) overpotential ($\eta_{10,OER}$) at 10 mA cm^{-2}, and (c) Tafel plots of Ni_3S_2/NF, $Ni_3(BO_3)_2$−Ni_3S_2/NF, $Ni_3(BO_3)_2$/NF, RuO_2/NF, and IrO_2/NF. (d) Schematic models of H_2O on the surfaces of $Ni_3(BO_3)_2$ and Ni_3S_2. (e) OER polarization curves of $Ni_3(BO_3)_2$−Ni_3S_2/NF in the first scan and after 3000 CV cycles in 1.0 M KOH. (f) Chronoamperometric tests at the potential of +1.45 V in a 1.0 M KOH electrolyte.

chemical desorption of the produced O_2, $OOH^* \rightarrow O_2 + H^+ + e^-$. The $Ni_3(BO_3)_2$−Ni_3S_2/NF electrode exhibited a low Tafel slope of 106.3 mV dec^{-1} (Figure 4c), demonstrating that the rate-determining step was the electrochemical desorption. This is likely because the electron-deficient $Ni_3(BO_3)_2$ on the electrode surface can effectively enhance the adsorption of oxygen-containing, Lewis base intermediates. Meanwhile, the S vacancies can also provide sufficient empty d orbitals to further enhance the bonding interactions with the oxygen-containing intermediates. One can see that the Tafel slope of $Ni_3(BO_3)_2$−Ni_3S_2/NF (106.3 mV dec^{-1}) was even lower than those of $Ni_3(BO_3)_2$/NF (128.8 mV dec^{-1}) and Ni_3S_2/NF (190.1 mV dec^{-1}) (Figure 4c), suggesting enhanced oxygen generation rate, as manifested in Figure 4a.

The turnover frequency (TOF) of OER (details in the Supporting Information) was also calculated at the overpotential of +300 mV, which was 0.12 s^{-1} for $Ni_3(BO_3)_2$−Ni_3S_2/NF, much higher than those for $Ni_3(BO_3)_2$/NF (0.07 s^{-1}) and Ni_3S_2/NF (0.06 s^{-1}). According to the results from DFT calculations (Figure 4d), the Gibbs adsorption energy of water (ΔG_{H_2O}) was +0.12 eV on Ni_3S_2, suggesting a hydrophobic surface. However, ΔG_{H_2O} became negative at −0.27 eV for $Ni_3(BO_3)_2$, indicative of hydrophilic characteristics. The results of DFT calculations suggest that the adsorption capacity of H_2O can be effectively improved by the formation of an amorphous (hydrophilic) $Ni_3(BO_3)_2$ layer. In addition, the amorphous layer can facilitate surface self-reconstruction forming a metal oxy(hydroxide) active layer with rich oxygen vacancies, a unique feature conducive to OER electrocatalysis.[24,25] In terms of stability tests (Figure 4e), after 3000 CV cycles, the $Ni_3(BO_3)_2$−Ni_3S_2/NF electrode exhibited only a minor attenuation. In the chronopotentiometric

https://dx.doi.org/10.1021/acsami.0c03796
ACS Appl. Mater. Interfaces 2020, 12, 23896−23903

measurements, the current density at the applied potential of +1.45 V remained almost unchanged during 30 h of continuous operation (Figure 4f), and the structure and composition of the catalysts were stable, as manifested in XRD and XPS (Figure S9) and SEM (Figure S10) measurements. This is likely because $Ni_3(BO_3)_2$ in the outer layer acted as a protective layer to impede internal erosion and enhance the catalyst stability during both HER and OER processes.

To clarify the synergistic effects between Ni_3S_2 and $Ni_3(BO_3)_2$ on the chemisorption of hydrogen and oxygen-containing intermediates, DFT calculations (details in the Supporting Information) were performed. The schematic models of $Ni_3(BO_3)_2$, Ni_3S_2, and $Ni_3(BO_3)_2$–Ni_3S_2 are shown in Figure 5a–c, respectively. Generally, for HER, the

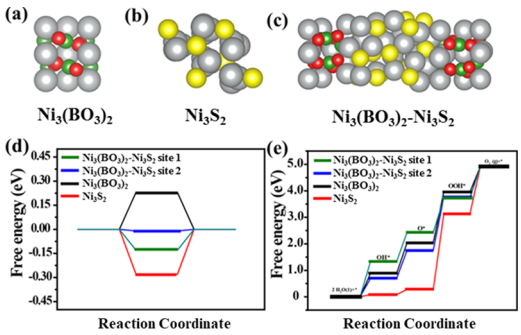

Figure 5. Schematic models of (a) $Ni_3(BO_3)_2$, (b) Ni_3S_2, and (c) $Ni_3(BO_3)_2$–Ni_3S_2 heterostructures. Gibbs free energy diagram for (d) HER and (e) OER on $Ni_3(BO_3)_2$, Ni_3S_2, and $Ni_3(BO_3)_2$–Ni_3S_2 heterostructure sites 1 and 2.

Gibbs adsorption energy of hydrogen (ΔG_{H^*}) on the catalyst surface is a key descriptor to evaluate the catalyst activity. A good HER catalyst should show a ΔG_{H^*} value close to zero.[43,44] The schematic models of H* intermediates on the surfaces of the $Ni_3(BO_3)_2$, Ni_3S_2, and $Ni_3(BO_3)_2$–Ni_3S_2 heterostructures are shown in Figures S12 and S13. As shown in Figure 5d and Table S4, ΔG_{H^*} at site 1 of the $Ni_3(BO_3)_2$–Ni_3S_2 heterostructures (Figure S12c) is about −0.13, and at site 2 it is −0.01 eV (Figure S13), both of which are much closer to the optimal ΔG_{H^*} of 0 eV than those of $Ni_3(BO_3)_2$ (+0.24 eV, Figure S12a) and Ni_3S_2 (−0.28 eV, Figure S12b). This suggests that the construction of a $Ni_3(BO_3)_2$–Ni_3S_2 heterostructure, with sites 1 and 2 being the likely active sites, improved the HER performances, as observed experimentally (Figure 3).

In addition, we calculated the free energy for each elementary step in OER, by constructing the schematic models of OH* (Figure S14), O* (Figure S15), and OOH* (Figure S16) intermediates on $Ni_3(BO_3)_2$, Ni_3S_2, and varied sites in $Ni_3(BO_3)_2$–Ni_3S_2. As shown in Figure 5e and Table S5, two most favorable sites in $Ni_3(BO_3)_2$–Ni_3S_2 heterostructures were identified, single $Ni_3(BO_3)_2$ and Ni_3S_2. It can be seen that the rate-determining step (RDS) for single $Ni_3(BO_3)_2$, Ni_3S_2, and site 2 of $Ni_3(BO_3)_2$–Ni_3S_2 was the third electron-transfer step, O* → OOH*, which has the highest endothermic energy, whereas the RDS of OER on site 1 of $Ni_3(BO_3)_2$–Ni_3S_2 was the first step, H_2O → OH*. To maximize the activity of OER, the uphill energy of the RDS should be as low as possible. From Figure 5e, one can see that the value of ΔG_{RDS} on site 1 of $Ni_3(BO_3)_2$–Ni_3S_2 (+1.34 eV) was significantly reduced, as compared to that on single $Ni_3(BO_3)_2$ (+1.91 eV) and Ni_3S_2 (+2.85 eV), and site 2 has a similar value (+1.99 eV) to $Ni_3(BO_3)_2$. These results indicate that the $Ni_3(BO_3)_2$–Ni_3S_2 heterostructure had a higher catalytic activity toward OER than $Ni_3(BO_3)_2$, and much higher than Ni_3S_2, in accordance with the experimental results (Figure 4). Clearly, the coupling of $Ni_3(BO_3)_2$ and Ni_3S_2 provides a unique interface that leads to improved electrocatalytic activities toward both HER and OER.

With the excellent OER and HER performance of the $Ni_3(BO_3)_2$–Ni_3S_2/NF heterostructures, the sample was utilized as a bifunctional electrocatalyst for overall water splitting in a two-electrode system in a 1.0 M KOH solution. From Figure 6a, one can see that the cell exhibited a low $E_{WS,10}$

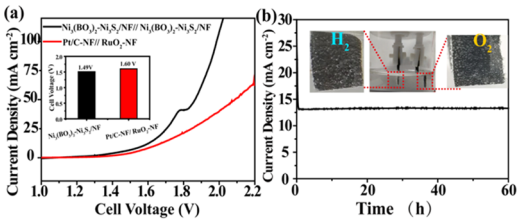

Figure 6. (a) Polarization curves and (b) long-term durability tests at 1.55 V for overall water splitting by $Ni_3(BO_3)_2$–Ni_3S_2/NF in a 1.0 M KOH solution. Inset to panel (a) is the cell voltage at 10 mA cm^{-2}, and inset to panel (b) are the photographs of the electrodes during overall water splitting.

of only 1.49 V, markedly lower than those based on commercial RuO_2/NF–Pt/NF electrodes (1.60 V, inset to Figure 6a) and relevant bifunctional electrocatalysts reported in the literature (Table S6). In fact, with the application of a 1.5 V battery, a large number of bubbles can be seen to form on the nickel foam and release slowly (Movie S1). Furthermore, during electrolysis at the applied voltage of 1.55 V for 30 h, a large number of H_2 and O_2 bubbles were produced on the electrode surface (inset to Figure 6b). The Faradaic efficiencies of HER and OER for the $Ni_3(BO_3)_2$–Ni_3S_2/NF sample were then calculated (Figure S17). At the applied potential of 1.55 V, the amount of H_2 gas generated was 3.91 μmol min^{-1}, which was very close to the theoretical value of 3.97 μmol min^{-1}, and the ratio of the H_2 and O_2 gas evolution rates was 3.91:1.97, close to the theoretical value of 2:1. These results demonstrated almost 100% faradaic efficiency of water splitting by the $Ni_3(BO_3)_2$–Ni_3S_2/NF heterostructures. The catalyst also exhibited outstanding durability in strong alkaline electrolytes with negligible degradation after 60 h of continuous operation (Figure 6b). Notably, ICP-AES measurements showed that after the long-term durability tests, none of the Ni, B, and S elements was found in the electrolyte solution, indicative of the robust structures of the heterostructured catalysts (Table S7).

CONCLUSIONS

In this study, a facile hydrothermal approach was described for the preparation of amorphous–crystalline $Ni_3(BO_3)_2$–Ni_3S_2 heterostructures as effective bifunctional electrocatalysts toward both HER and OER. The amorphous $Ni_3(BO_3)_2$ was found to enhance the Lewis base adsorption due to Lewis acid–base interactions, which, together with the S vacancies, facilitated chemisorption for both hydrogen and oxygen-containing intermediates. This was confirmed by results from DFT calculations. Remarkably, the electrocatalytic perform-

https://dx.doi.org/10.1021/acsami.0c03796
ACS Appl. Mater. Interfaces 2020, 12, 23896–23903

ance toward overall water splitting was even better than those based on the commercial Pt/C and RuO_2 catalysts. Results from this study highlight the significance of rational design and engineering of interfaces and heterostructures in the development of high-performance electrocatalysts for electrochemical energy technologies.

■ ASSOCIATED CONTENT

Supporting Information

The Supporting Information is available free of charge at https://pubs.acs.org/doi/10.1021/acsami.0c03796.

Additional electrochemical and computational details; XRD, XPS spectra; SEM, TEM, and HRTEM images; LSV curves of hydrogen electrode reactions on a Pt wire, and additional data for HER and OER, cyclic voltammetry curves and ECSA; schematic models of various adsorption sites, and comparison of HER, OER, and water splitting activity (PDF)

Large number of bubbles can be seen to form on the nickel foam and release slowly (MP4)

■ AUTHOR INFORMATION

Corresponding Authors

Genban Sun − *Beijing Key Laboratory of Energy Conversion and Storage Materials Institute, College of Chemistry, Beijing Normal University, Beijing 100875, China;* orcid.org/0000-0001-9005-8123; Email: gbsun@bnu.edu.cn

Jia Zhu − *Key Laboratory of Theoretical and Computational Photochemistry, Ministry of Education, Beijing Normal University, Beijing 100875, China;* orcid.org/0000-0002-4938-2850; Email: zhu.jia@bnu.edu.cn

Shaowei Chen − *Department of Chemistry and Biochemistry, University of California, Santa Cruz, California 95060, United States;* orcid.org/0000-0002-3668-8551; Email: shaowei@ucsc.edu

Authors

Zemin Sun − *Beijing Key Laboratory of Energy Conversion and Storage Materials Institute, College of Chemistry, Beijing Normal University, Beijing 100875, China*

Xiaorui Wang − *Key Laboratory of Theoretical and Computational Photochemistry, Ministry of Education, Beijing Normal University, Beijing 100875, China*

Mengwei Yuan − *Beijing Key Laboratory of Energy Conversion and Storage Materials Institute, College of Chemistry, Beijing Normal University, Beijing 100875, China*

Han Yang − *Beijing Key Laboratory of Energy Conversion and Storage Materials Institute, College of Chemistry, Beijing Normal University, Beijing 100875, China*

Yuhe Su − *Beijing Key Laboratory of Energy Conversion and Storage Materials Institute, College of Chemistry, Beijing Normal University, Beijing 100875, China*

Kefan Shi − *Beijing Key Laboratory of Energy Conversion and Storage Materials Institute, College of Chemistry, Beijing Normal University, Beijing 100875, China*

Caiyun Nan − *Beijing Key Laboratory of Energy Conversion and Storage Materials Institute, College of Chemistry, Beijing Normal University, Beijing 100875, China*

Huifeng Li − *Beijing Key Laboratory of Energy Conversion and Storage Materials Institute, College of Chemistry, Beijing Normal University, Beijing 100875, China;* orcid.org/0000-0002-0257-3967

Xiaojing Yang − *Beijing Key Laboratory of Energy Conversion and Storage Materials Institute, College of Chemistry, Beijing Normal University, Beijing 100875, China;* orcid.org/0000-0003-3620-3507

Complete contact information is available at: https://pubs.acs.org/10.1021/acsami.0c03796

Author Contributions

Z.S., X.W., and M.Y. contributed equally to the work. The manuscript was written through contributions of all authors. All authors have given approval to the final version of the manuscript.

Notes

The authors declare no competing financial interest.

■ ACKNOWLEDGMENTS

This project was supported by the National Natural Science Foundations of China (21771024, 21606021, and 21871028). S.W.C. thanks the National Science Foundation (CHE-1900235) for partial support of the work.

■ REFERENCES

(1) Larcher, D.; Tarascon, J.-M. Towards Greener and More Sustainable Batteries for Electrical Energy Storage. *Nat. Chem.* **2015**, *7*, 19−29.

(2) Chu, S.; Majumdar, A. Opportunities and Challenges for a Sustainable Energy Future. *Nature* **2012**, *488*, 294−303.

(3) Feng, X.; Maier, S.; Salmeron, M. Water Splits Epitaxial Graphene and Intercalates. *J. Am. Chem. Soc.* **2012**, *134*, 5662−5668.

(4) Lu, B.; Guo, L.; Wu, F.; Peng, Y.; Lu, J. E.; Smart, T. J.; Wang, N.; Finfrock, Y. Z.; Morris, D.; Zhang, P.; Li, N.; Gao, P.; Ping, Y.; Chen, S. Ruthenium Atomically Dispersed in Carbon Outperforms Platinum toward Hydrogen Evolution in Alkaline Media. *Nat. Commun.* **2019**, *10*, No. 631.

(5) Zheng, Y.; Jiao, Y.; Zhu, Y.; Li, L. H.; Han, Y.; Chen, Y.; Jaroniec, M.; Qiao, S.-Z. High Electrocatalytic Hydrogen Evolution Activity of an Anomalous Ruthenium Catalyst. *J. Am. Chem. Soc.* **2016**, *138*, 16174−16181.

(6) Jian, J.; Yuan, L.; Qi, H.; Sun, X.; Zhang, L.; Li, H.; Yuan, H.; Feng, S. Sn−Ni_3S_2 Ultrathin Nanosheets as Efficient Bifunctional WaterSplitting Catalysts with a Large Current Density and Low Overpotential. *ACS Appl. Mater. Interfaces* **2018**, *10*, 40568−40576.

(7) Pandey, A.; Mukherjee, A.; Chakrabarty, S.; Chanda, D.; Basu, S. Interface Engineering of an RGO/MoS_2/Pd 2D Heterostructure for Electrocatalytic Overall Water Splitting in Alkaline Medium. *ACS Appl. Mater. Interfaces* **2019**, *11*, 42094−42103.

(8) Lin, L.; Sun, Z.; Yuan, M.; He, J.; Long, R.; Li, H.; Nan, C.; Sun, G.; Ma, S. Significant Enhancement of the Performance of Hydrogen Evolution Reaction through Shape-Controlled Synthesis of Hierarchical Dendrite-Like Platinum. *J. Mater. Chem. A* **2018**, *6*, 8068−8077.

(9) Lin, L.; Sun, Z.; Yao, H.; Yuan, M.; Yang, H.; Li, H.; Zhang, Q.; Wang, D.; Gu, L.; Sun, G.; Zhu, J.; Fang, W.; Tang, Z. Tuning Surface Lattice Strain toward a Pt−Skin $CoPt_x$ Truncated Octahedron for Hydrogen Evolution Reaction. *J. Phys. Chem. C* **2019**, *123*, 29722−29728.

(10) Cobo, S.; Heidkamp, J.; Jacques, P.-A.; Fize, J.; Fourmond, V.; Guetaz, L.; Jousselme, B.; Ivanova, V.; Dau, H.; Palacin, S.; Fontecave, M.; Artero, V. A Janus Cobalt-Based Catalytic Material for Electro-Splitting of Water. *Nat. Mater.* **2012**, *11*, 802−807.

(11) You, B.; Jiang, N.; Sheng, M.; Bhushan, M. W.; Sun, Y. Hierarchically Porous Urchin-Like Ni_2P Superstructures Supported on Nickel Foam as Efficient Bifunctional Electrocatalysts for Overall Water Splitting. *ACS Catal.* **2016**, *6*, 714−721.

(12) Sun, Z.; Yuan, M.; Yang, H.; Lin, L.; Jiang, H.; Ge, S.; Li, H.; Sun, G.; Ma, S.; Yang, X. 3D Porous Amorphous γ-CrOOH on Ni

Foam as Bifunctional Electrocatalyst for Overall Water Splitting. *Inorg. Chem.* **2019**, *58*, 4014−4018.
(13) Sun, Z.; Yuan, M.; Lin, L.; Yang, H.; Li, H.; Sun, G.; Yang, X.; Ma, S. Needle Grass-Like Cobalt Hydrogen Phosphate on Ni foam as an Effective and Stable Electrocatalyst for the Oxygen Evolution Reaction. *Chem. Commun.* **2019**, *55*, 9729−9732.
(14) Xu, Q.; Jiang, H.; Zhang, H.; Hu, Y.; Li, C. Heterogeneous Interface Engineered Atomic Configuration on Ultrathin $Ni(OH)_2$/Ni_3S_2 Nanoforests for Efficient Water Splitting. *Appl. Catal., B* **2019**, *242*, 60−66.
(15) Sun, Z.; Lin, L.; Nan, C.; Li, H.; Sun, G.; Yang, X. Amorphous Boron Oxide Coated NiCo Layered Double Hydroxide Nanoarrays for Highly Efficient Oxygen Evolution Reaction. *ACS Sustainable Chem. Eng.* **2018**, *6*, 14257−14263.
(16) Zhang, G.; Feng, Y.-S.; Lu, W.-T.; He, D.; Wang, C.-Y.; Li, Y.-K.; Wang, X.-Y.; Cao, F.-F. Enhanced Catalysis of Electrochemical Overall Water Splitting in Alkaline Media by Fe Doping in Ni_3S_2 Nanosheet Arrays. *ACS Catal.* **2018**, *8*, 5431−5441.
(17) Chen, P.; Zhou, T.; Zhang, M.; Tong, Y.; Zhong, C.; Zhang, N.; Zhang, L.; Wu, C.; Xie, Y. 3D Nitrogen-Anion-Decorated Nickel Sulfides for Highly Efficient Overall Water Splitting. *Adv. Mater.* **2017**, *29*, No. 1701584.
(18) Niu, W.; Li, L.; Liu, X.; Wang, N.; Liu, J.; Zhou, W.; Tang, Z.; Chen, S. Mesoporous N-Doped Carbons Prepared with Thermally Removable Nanoparticle Templates: An Efficient Electrocatalyst for Oxygen Reduction Reaction. *J. Am. Chem. Soc.* **2015**, *137*, 5555−5562.
(19) Shit, S.; Chhetri, S.; Jang, W.; Murmu, N. C.; Koo, H.; Samanta, P.; Kuila, T. Cobalt Sulfide/Nickel Sulfide Heterostructure Directly Grown on Nickel Foam: An Efficient and Durable Electrocatalyst for Overall Water Splitting Application. *ACS Appl. Mater. Interfaces* **2018**, *10*, 27712−27722.
(20) Zhou, W.; Wu, X.-J.; Cao, X.; Huang, X.; Tan, C.; Tian, J.; Liu, H.; Wang, J.; Zhang, H. Ni_3S_2 Nanorods/Ni Foam Composite Electrode with Low Overpotential for Electrocatalytic Oxygen Evolution. *Energy Environ. Sci* **2013**, *6*, 2921−2924.
(21) Zhang, J.; Wang, T.; Pohl, D.; Rellinghaus, B.; Dong, R.; Liu, S.; Zhuang, X.; Feng, X. Interface Engineering of MoS_2/Ni_3S_2 Heterostructures for Highly Enhanced Electrochemical Overall-Water-Splitting Activity. *Angew. Chem., Int. Ed.* **2016**, *55*, 6702−6707.
(22) Zheng, M.; Guo, K.; Jiang, W.-J.; Tang, T.; Wang, X.; Zhou, P.; Du, J.; Zhao, Y.; Xu, C.; Hu, J.-S. When MoS_2 Meets Feooh: A "One-Stone-Two-Birds" Heterostructure as a Ifunctional Electrocatalyst for Efficient Alkaline Water Splitting. *Appl. Catal., B* **2019**, *244*, 1004−1012.
(23) Gong, Y.; Yang, Z.; Lin, Y.; Wang, J.; Pan, H.; Xu, Z. Hierarchical Heterostructure $NiCO_2O_4$@$CoMoO_4$/NF as an Efficient Bifunctional Electrocatalyst for Overall Water Splitting. *J. Mater. Chem. A* **2018**, *6*, 16950−16958.
(24) Duan, Y.; Yu, Z.-Y.; Hu, S.-J.; Zheng, X.-S.; Zhang, C.-T.; Ding, H.-H.; Hu, B.-C.; Fu, Q.-Q.; Yu, Z.-L.; Zheng, X.; Zhu, J.-F.; Gao, M.-R.; Yu, S.-H. Scaled-Up Synthesis of Amorphous NiFeMo Oxides and Their Rapid Surface Reconstruction for Superior Oxygen Evolution Catalysis. *Angew. Chem., Int. Ed.* **2019**, *58*, 15772−15777.
(25) Zhang, B.; Jiang, K.; Wang, H.; Hu, S. Fluoride-Induced Dynamic Surface Self-Reconstruction Produces Unexpectedly Efficient Oxygen-Evolution Catalyst. *Nano Lett.* **2019**, *19*, 530−537.
(26) Dong, C.; Kou, T.; Gao, H.; Peng, Z.; Zhang, Z. Eutectic-Derived Mesoporous Ni-Fe-O Nanowire Network Catalyzing Oxygen Evolution and Overall Water Splitting. *Adv. Energy Mater.* **2018**, *8*, No. 1701347.
(27) Yang, N.; Tang, C.; Wang, K.; Du, G.; Asiri, A. M.; Sun, X. Iron-Doped Nickel Disulfide Nanoarray: a Highly Efficient and Stable Electrocatalyst for Water Splitting. *Nano Res.* **2016**, *9*, 3346−3354.
(28) Zhang, H.; Jiang, H.; Hu, Y.; Li, Y.; Xu, Q.; Petr, S.; Li, C. Tailorable Surface Sulfur Chemistry of Mesoporous Ni_3S_2 Particles for Efficient Oxygen Evolution. *J. Mater. Chem. A* **2019**, *7*, 7548−7552.
(29) Liu, Q.; Huang, J.; Zhao, Y.; Cao, L.; Li, K.; Zhang, N.; Yang, D.; Feng, L.; Feng, L. Tuning The Coupling Interface of Ultrathin Ni_3S_2@NiV-LDH Heterogeneous Nanosheet Electrocatalysts For Improved Overall Water Splitting. *Nanoscale* **2019**, *11*, 8855−8863.
(30) An, L.; Zhang, Z.; Feng, J.; Lv, F.; Li, Y.; Wang, R.; Lu, M.; Gupta, R. B.; Xi, P.; Zhang, S. Heterostructure-Promoted Oxygen Electrocatalysis Enables Rechargeable Zinc−Air Battery with Neutral Aqueous Electrolyte. *J. Am. Chem. Soc.* **2018**, *140*, 17624−17631.
(31) Yang, Y.; Zhang, K.; Lin, H.; Li, X.; Chan, H. C.; Yang, L.; Gao, Q. MoS_2−Ni_3S_2 Heteronanorods as Efficient and Stable Bifunctional Electrocatalysts for Overall Water Splitting. *ACS Catal.* **2017**, *7*, 2357−2366.
(32) Liu, N.; Yang, L.; Wang, S.; Zhong, Z.; He, S.; Yang, X.; Gao, Q.; Tang, Y. Ultrathin MoS_2 Nanosheets Growing Within an In-Situ-Formed Template as Efficient Electrocatalysts for Hydrogen Evolution. *J. Power Sources* **2015**, *275*, 588−594.
(33) Liu, N.; Guo, Y.; Yang, X.; Lin, H.; Yang, L.; Shi, Z.; Zhong, Z.; Wang, S.; Tang, Y.; Gao, Q. Microwave-Assisted Reactant-Protecting Strategy toward Efficient MoS_2 Electrocatalysts in Hydrogen Evolution Reaction. *ACS Appl. Mater. Interfaces* **2015**, *7*, 23741−23749.
(34) Guo, F.; Wu, Y.; Chen, H.; Liu, Y.; Yang, L.; Ai, X.; Zou, X. High-Performance Oxygen Evolution Electrocatalysis by Boronized Metal Sheets with Self-Functionalized Surfaces. *Energy Environ. Sci.* **2019**, *12*, 684−692.
(35) An, L.; Li, Y.; Luo, M.; Yin, J.; Zhao, Y.-Q.; Xu, C.; Cheng, F.; Yang, Y.; Xi, P.; Guo, S. Atomic-Level Coupled Interfaces and Lattice Distortion on CuS/NiS_2 Nanocrystals Boost Oxygen Catalysis for Flexible Zn-Air Batteries. *Adv. Funct. Mater.* **2017**, *27*, No. 1703779.
(36) Zheng, X.; Zhang, Y.; Liu, H.; Fu, D.; Chen, J.; Wang, J.; Zhong, C.; Deng, Y.; Han, X.; Hu, W. In Situ Fabrication of Heterostructure on Nickel Foam with Tuned Composition for Enhancing Water-Splitting Performance. *Small* **2018**, *14*, No. 1803666.
(37) Sun, Z.; He, J.; Yuan, M.; Lin, L.; Zhang, Z.; Kang, Z.; Liao, Q.; Li, H.; Sun, G.; Yang, X.; Long, R.; Zhang, Y. Li^+-Clipping for Edge S-Vacancy MoS_2 Quantum Dots as an Efficient Bifunctional Electrocatalyst Enabling Discharge Growth of Amorphous Li_2O_2 Film. *Nano Energy* **2019**, *65*, No. 103996.
(38) Durst, J.; Siebel, A.; Simon, C.; Hasché, F.; Herranz, J.; Gasteiger, H. A. New Insights Into the Electrochemical Hydrogen Oxidation and Evolution Reaction Mechanism. *Energy Environ. Sci.* **2014**, *7*, 2255−2260.
(39) Islam, M. S.; Kim, M.; Jin, X.; Oh, S. M.; Lee, N.-S.; Kim, H.; Hwang, S.-J. Bifunctional 2D Superlattice Electrocatalysts of Layered Double Hydroxide-Transition Metal Dichalcogenide Active for Overall Water Splitting. *ACS Energy Lett.* **2018**, *3*, 952−960.
(40) Sun, Y.; Gao, S.; Lei, F.; Xie, Y. Atomically-Thin Two-Dimensional Sheets for Understanding Active Sites in Catalysis. *Chem. Soc. Rev.* **2015**, *44*, 623−636.
(41) Zeng, L.; Sun, K.; Wang, X.; Liu, Y.; Pan, Y.; Liu, Z.; Cao, D.; Song, Y.; Liu, S.; Liu, C. Three-Dimensional-Networked Ni_2P/Ni_3S_2 Heteronanoflake Arrays for Highly Enhanced Electrochemical Overall-Water-Splitting Activity. *Nano Energy* **2018**, *51*, 26−36.
(42) Zhang, G.; Feng, Y.-S.; Lu, W. T.; He, D.; Wang, C.-Y.; Li, Y.-K.; Wang, X.-Y.; Cao, F. F. Enhanced Catalysis of Electrochemical Overall Water Splitting in Alkaline Media by Fe Doping in Ni_3S_2 Nanosheet Arrays. *ACS Catal.* **2018**, *8*, 5431−5441.
(43) Nørskov, J. K.; Bligaard, T.; Logadottir, A.; Kitchin, J. R.; Chen, J. G.; Pandelov, S.; Stimming, U. Trends in the Exchange Current for Hydrogen Evolution. *J. Electrochem. Soc.* **2005**, *152*, J23−J26.
(44) Tang, Q.; Jiang, D.-e. Mechanism of Hydrogen Evolution Reaction on 1T-MoS_2 from First Principles. *ACS Catal.* **2016**, *6*, 4953−4961.

https://dx.doi.org/10.1021/acsami.0c03796
ACS Appl. Mater. Interfaces 2020, 12, 23896−23903